Sedimentary Geology 403 (2020) 105653

Contents lists available at ScienceDirect

Sedimentary Geology

journal homepage: www.elsevier.com/locate/sedgeo

Abrasion of detrital grain-coating clays during sediment transport: Implications for diagenetic clay coats

Iris T.E. Verhagen [a,*], Adriana Crisóstomo-Figueroa [b], James E.P. Utley [a], Richard H. Worden [a]

[a] University of Liverpool, Department of Earth, Ocean and Ecological Sciences, Jane Herdman Building, 4 Brownlow Street, Liverpool, L69 3GP, United Kingdom
[b] University of Leeds, School of Earth and Environment, Leeds, LS2 9JT, United Kingdom

ARTICLE INFO

Article history:
Received 20 January 2020
Received in revised form 23 March 2020
Accepted 24 March 2020
Available online 29 March 2020

Editor: Dr. J. Knight

Keywords:
Grain-coating clays
Abrasion
Sediment transport
Reservoir quality
Diagenesis

ABSTRACT

Detrital grain-coating clay minerals have been identified as precursors of diagenetic grain-coating clay minerals that inhibit quartz cementation and preserve good reservoir quality properties in deeply buried sandstone reservoirs. Between initial and final deposition, detrital grain coats are likely to be affected by sediment transport processes. To date, it has not been demonstrated that detrital grain-coating clays are able to survive sediment transport. Flume experiments simulating open-channel flow conditions were performed using sediments from the Ravenglass estuary (Cumbria, UK), where the distribution and characteristics of modern detrital grain-coating clays is well established. Scanning electron microscopy and automated mineralogy techniques were employed to study the sediment before and after transport to determine the stability of the detrital grain-coating clays. The experimental results show that detrital grain-coating clays are still present after sediment transport in turbulent flows with velocities up to 0.5 m s^{-1}. The stability of the detrital grain-coating clays was enhanced by (1) high initial clay coat coverage, (2) turbulence characteristics of the flow, and (3) entrapment of the detrital grain-coating clays in bedforms. This work documents the first quantifiable evidence that estuary-derived, detrital clay coats are routinely preserved after sediment transport. Clay coat-rich estuarine sediments can therefore act as the source of clay coated grains found in cleaner estuarine sandstones and may even survive transport out into open marine settings.

1. Introduction

The relationship between reservoir quality and diagenetic grain-coating clay minerals, which inhibit quartz cementation but can also block pore throats, is well established (e.g., Heald and Larese, 1974; Ehrenberg, 1993; Bloch et al., 2002; Worden and Morad, 2003; Taylor et al., 2010; Ajdukiewicz and Larese, 2012). Diagenetic chlorite coats, predominantly found in estuarine-deltaic sandstones, are the most effective coats for the preservation of reservoir quality (Dowey et al., 2012; Worden et al., n.d). Illite coats, although less effective than chlorite (Bloch et al., 2002), have been reported to have a positive effect on porosity in reservoir sandstones of the Garn Formation (North Sea) (Storvoll et al., 2002) and Norphlet Formation (Ajdukiewicz et al., 2010). Molenaar and Felder (2018) demonstrated that the illite cements in Rotliegend sandstones do not distinctly influence porosity due to their small volume, but they significantly reduce permeability. Grain-coating kaolinite found in Rotliegend sandstones have a positive effect on porosity if the coats are thin and inhibit quartz cement, but they strongly reduce permeability if they are thick and dense (Waldmann and Gaupp, 2016).

Morphologically, the coverage of the authigenic clay mineral coat around the grain is key in limiting the growth of authigenic quartz cement, and even small breaks in the coat can lead to quartz cementation (Bloch et al., 2002; Billault et al., 2003; Worden et al., n.d). Grain size also controls the effectiveness of the grain-coating clay minerals because in finer grained sediment the clay coats have to cover a larger surface area relative to coarser grained sediments (Bloch et al., 2002).

Diagenetic grain-coating clay minerals have been linked to detrital precursor coats through several different mechanisms, including direct growth on the detrital clays or reactions between kaolinite and K-feldspar (Ajdukiewicz et al., 2010; Ajdukiewicz and Larese, 2012; Molenaar and Felder, 2018), and through thermally driven recrystallisation of Al- and Fe-rich precursor coats (Ehrenberg, 1993; Aagaard et al., 2000; Ajdukiewicz and Larese, 2012; Worden et al., n.d).

Multiple processes have been proposed to explain detrital grain-coating clay formation: infiltration of clays through the vadose zone whilst saturated with rainwater (Matlack et al., 1989; Moraes and De Ros, 1990), inherited grain-coating clays (Wilson, 1992), flocculation of mud (Worden and Morad, 2003), bioturbation and feeding activity of worms (Needham et al., 2005; Worden et al., 2006), and attachment

* Corresponding author.
E-mail address: verhagen@liverpool.ac.uk (I.T.E. Verhagen).

https://doi.org/10.1016/j.sedgeo.2020.105653

through cohesive biofilms (Wooldridge et al., 2017a). Recent studies of detrital clay in modern marginal marine environments have concluded that grain size and clay fraction of the sediment are the main controls on clay coat distribution (Dowey et al., 2017; Wooldridge et al., 2017b; Daneshvar and Worden, 2018).

Regardless of the mechanism by which detrital clay coats form, it is likely that they are subjected to sediment transport processes prior to final deposition and subsequent burial. Although inherited coats have been recognised in reservoir sandstones (Houseknecht and Ross Jr., 1992; Wilson, 1992; Bloch et al., 2002; Anjos et al., 2003; Ajdukiewicz et al., 2010), these observations were, to date, based solely on microscope analysis. Laboratory flume experiments have been routinely used to study flow and bedform dynamics in a wide range of depositional environments including rivers, deltas, and deep marine settings (e.g. Leclair and Bridge, 2001; Baas and Best, 2002; Baas et al., 2011; Muto et al., 2012; Verhagen et al., 2013; Cartigny et al., 2014). This study uses open-channel flow experiments to investigate the stability of detrital grain-coating clays during sediment transport. The potential for, and controls on, clay coat preservation are discussed and linked to predicted reservoir quality in buried estuarine sandstones.

2. Geological setting

The Ravenglass estuary, located in Cumbria (NW England; Fig. 1), covers a 5.6 km^2 area of which 86% is intertidal with a wide range of depositional environments, including tidal bars, dunes, tidal flats, and salt marshes (Bousher, 1999; Lloyd et al., 2013; Wooldridge et al., 2017b; Daneshvar and Worden, 2018; Griffiths et al., 2018, 2019a, 2019b; Wooldridge et al., 2018, 2019b).

The rivers Irt, Mite and Esk feed the estuary and supply chlorite- and illite-rich sediment from the hinterland and surrounding surficial glacial tills (Bousher, 1999; Griffiths et al., 2019b). Estuarine sediments are dominated by quartz, feldspar, muscovite, carbonate and Fe-rich minerals (e.g., lithic chlorite, pyrite), as well as clay minerals (Daneshvar and Worden, 2018). Of the clay minerals, illite is the most abundant, particularly in the fine-grained depositional settings in the inner and central basin of the estuary (Griffiths et al., 2019b).

The mineralogy, morphology and abundance of grain-coating clays in the Ravenglass estuary has been studied in detail (Wooldridge et al., 2017b, 2019a). Wooldridge et al. (2017b) documented the first high resolution characterisation of modern, detrital grain-coating clays and proposed this as an analogue for diagenetic grain-coating clays that occur in deeply buried, marginal marine sandstone reservoirs. The sedimentary environment is identified as the main control on the detrital grain-coating clay coverage and intergranular bridges, ridges, and clumps are recognised as the main textures of the coats (Wooldridge et al., 2017b). The coats themselves are predominantly composed of illite, but also contain kaolinite and chlorite (Wooldridge et al., 2017b, 2019a).

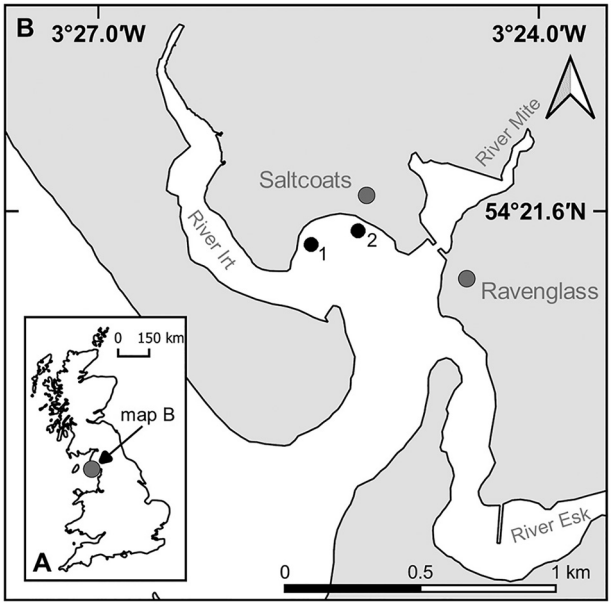

Fig. 1. Overview map (A) shows the location of the Ravenglass estuary in Cumbria (UK), (B) highlights the sample locations 1 and 2. Coordinates are in WGS84 and the figure contains data from ©2018 Google and ©OpenStreetMap contributors.

3. Methods

3.1. Flume experiments

Seven flume experiments were conducted in an HM 166 GUNT Hamburg flume tank at The University of Liverpool, UK. The flume has a semi-circular flow channel with a paddle wheel that controls the flow velocity and a lowered section in the channel to create a sediment bed (Fig. 2). Sediments used in the experiments were collected from the surface (i.e., top 5 cm) at two mixed sand- and mud-flat localities (between 75 and 90% sand and 10–25% mud) near Saltcoats hamlet in the Ravenglass estuary (Fig. 1). This sediment has been fully characterised by Wooldridge et al. (2017a, 2017b) and Griffiths et al. (2019ba,b). The mineralogical composition of the sediment at the two localities is almost identical, with a < 1% difference between the components measured with automated mineralogy techniques. Therefore, experiments using sediment from both localities are directly comparable. Prior to filling the flume with tap water, a pre-transport surface sediment sample was taken (Fig. 2B). The water salinity profile in the Ravenglass estuary varies with each tidal cycle and proximity to the sea (Daneshvar, 2015) as well as changes in the weather (river runoff). Water salinity influences the behaviour, in particular flocculation, of clay particles by affecting their surface charge (Coussot, 1997). Flow velocity and associated turbulence also affects the break-up and aggradation of flocs (Winterwerp, 2002; Manning et al., 2010). Due to this complex interplay of salinity and flow velocity on the behaviour of clay particles, tap water was chosen as a first approximation of the mostly low salinity conditions that are expected at the sample locality (>1 km upstream of the estuary mouth; Daneshvar, 2015).

Two Nixon Streamflo velocity meters were used to measure the flow velocity at 0.5 and 4 cm above the sediment bed (Fig. 2C). The velocity meters have an operational range between 0.05 and 1.5 m s^{-1}, with an accuracy of ±2%, and display the average flow velocity over 10 s intervals.

Flow velocities were set to range between 0.20 and 0.55 m s^{-1} based on a trial experiment (Table 1). Below 0.20 m s^{-1} no sediment movement was observed and 0.55 m s^{-1} was the maximum flow velocity reached by the flume tank. This velocity range fits well with velocities recorded and modelled during estuarine circulation in previous studies (Amos et al., 1998; Christie and Dyer, 1998; Kornman and De Deckere, 1998; Widdows et al., 1998; Wood et al., 1998; Winterwerp et al., 2006; Brown and Davies, 2010). At the start of each experiment the flow velocity was increased in steps using the paddle speed adjustment dial, each step corresponding to an increase in flow velocity of approximately 0.05 m s^{-1}. The flow was allowed to stabilise for three minutes before the next stepped increase. When the target velocity was reached, it was kept constant for 60 min in experiments 1–4 and 7 (Fig. 3A-C). In experiments 5 and 6 the velocity was varied over a 140-min period (Fig. 3D). At the end of each experiment the velocity was reduced, again in three-minute steps. During acceleration and deceleration, the flow velocity was recorded every minute, during the intervals of constant flow velocity measurements were taken every three minutes. The paddle wheel itself moves in the flow and interacts with the suspended grains, but this effect is assumed to be minimal compared to grain-to-grain collisions in the flow (Wilson, 1992).

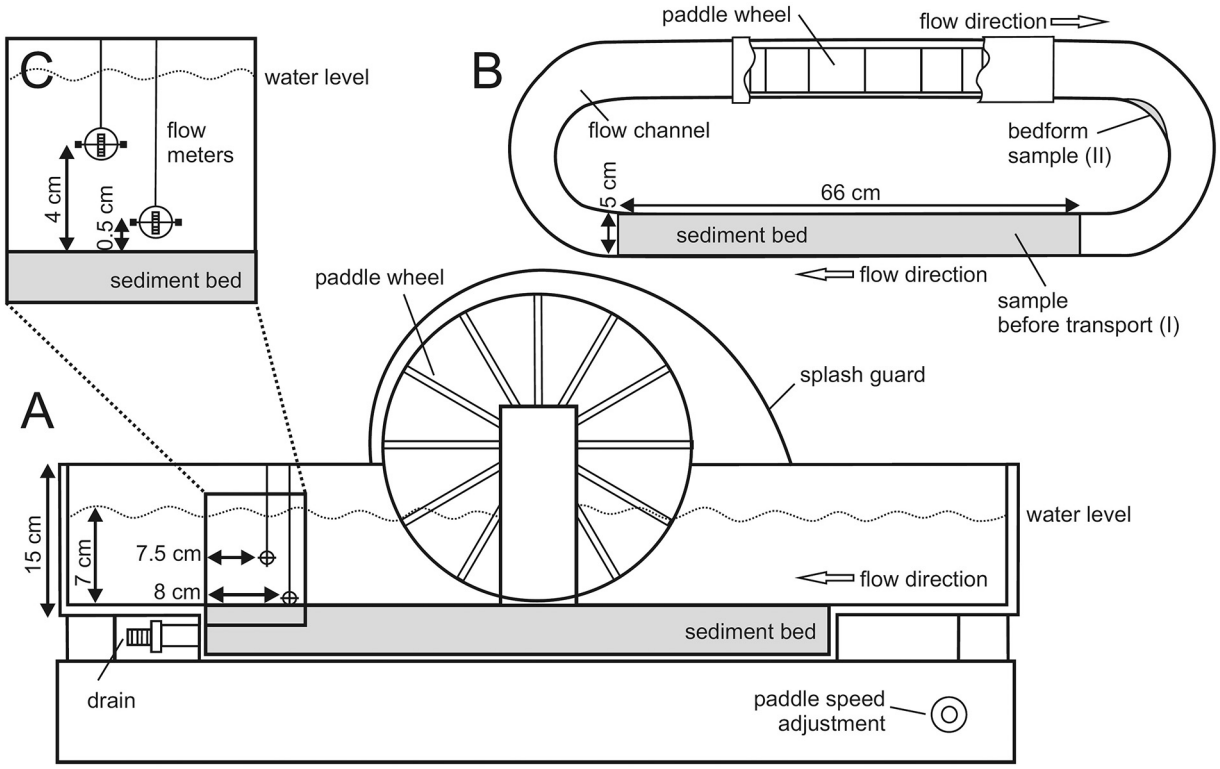

Fig. 2. Schematic diagrams of the flume set-up used in this study (not to scale). (A) The flume tank consists of a transparent plexiglass flow channel, a 5 cm deep sediment bed section, and a paddle wheel to control the flow velocity. (B) Plan view of the flume shows dimensions of the sediment bed, the flow direction, and the surface sample locations before (I) and after (II) the experiments. (C) Detailed view of the Nixon Streamflo velocity meter set-up. Figure adapted from the HM166 data sheet (G.U.N.T. Hamburg, 2018).

To establish the fluid flow characteristics, Froude (*Fr*) and Reynolds (*Re*) numbers were calculated for each experiment (Table 1) using the following equations respectively:

$$Fr = \frac{\bar{U}}{\sqrt{(gh)}}, \quad (1)$$

$$Re = \frac{\bar{U}h\rho}{\mu}, \quad (2)$$

where $\bar{U}$ is the average flow velocity calculated over the intervals with constant flow velocity (Fig. 3), g is the gravitational acceleration (9.81 m s^{-2}), h is the flow depth (m), ρ the density of the water (20 °C, 998.2 kg m^{-3}), and μ the dynamic viscosity of water (20 °C, 0.001 Ns m^{-2}).

Apart from velocity measurements, photographs and videos were collected during the experiments using the camera of an Apple Inc. iPhone 6 (8 MP and 1080p video) to study flow behaviour, sedimentary structures and modes of grain motion in detail. After each experiment the sediment was left to settle for 60 min before the flume tank was drained and a sample was taken from the new bedform that formed downstream of the paddle wheel (Fig. 2B).

3.2. Analytical techniques

The sediment samples, taken before and after the experiments, were dried at room temperature and impregnated with Epofix® resin to create polished blocks. The blocks were carbon-coated and analysed using automated mineralogy (Scanning Electron Microscopy-Energy Dispersive Spectroscopy, SEM-EDS) and backscattered electron microscopy (BSEM).

SEM-EDS analysis was conducted using a FEI WellSite QEMSCAN® system (FEI Company, Hillsboro, OR, USA), operating with a 15 kV acceleration voltage and ~5 nA beam current. The electron beam excites the sample that then emits secondary X-rays that are recorded by two Bruker energy dispersive X-ray spectrometers (EDS) at a 2 μm

Table 1
Overview of the experimental data displaying the total duration, the mean ($\bar{U}$), minimum (U_{min}) and maximum (U_{max}) velocity in m s^{-1} measured 0.5 and 4 cm above the sediment bed (see Fig. 3), the standard deviation (σ) and the Froude (*Fr*) and Reynolds (*Re*) numbers calculated using the mean velocities (Eqs. 1 and 2) for each experiment.

		0.5 cm						4 cm					
Experiment #	Duration (min)	$\bar{U}$ (m s^{-1})	U_{min} (m s^{-1})	U_{max} (m s^{-1})	σ	*Fr*	*Re*	$\bar{U}$ (m s^{-1})	U_{min} (m s^{-1})	U_{max} (m s^{-1})	σ	*Fr*	*Re*
1	73	0.29	0.27	0.30	0.01	0.35	20,159	0.31	0.30	0.33	0.01	0.38	21,932
2	73	0.31	0.23	0.33	0.02	0.38	21,957	0.35	0.30	0.36	0.02	0.42	24,337
3	79	0.35	0.33	0.37	0.01	0.42	24,526	0.39	0.37	0.42	0.02	0.47	27,397
4	79	0.35	0.33	0.36	0.01	0.42	24,120	0.39	0.38	0.41	0.01	0.48	27,513
5a		0.21	0.15	0.24	0.03	0.25	14,436	0.27	0.26	0.29	0.01	0.33	18,852
5b	140	0.43	0.40	0.47	0.02	0.51	29,720	0.48	0.46	0.50	0.01	0.58	33,843
5c		0.13	0.11	0.15	0.01	0.16	9229	0.22	0.16	0.24	0.03	0.27	15,531
6a		0.21	0.20	0.22	0.01	0.26	14,778	0.27	0.26	0.30	0.01	0.32	18,597
6b	139	0.47	0.46	0.47	0.00	0.57	32,827	0.48	0.47	0.48	0.00	0.58	33,389
6c		0.19	0.18	0.19	0.00	0.23	13,059	0.22	0.22	0.23	0.00	0.27	15,596
7	89	0.44	0.42	0.47	0.02	0.54	31,061	0.48	0.46	0.49	0.01	0.58	33,476

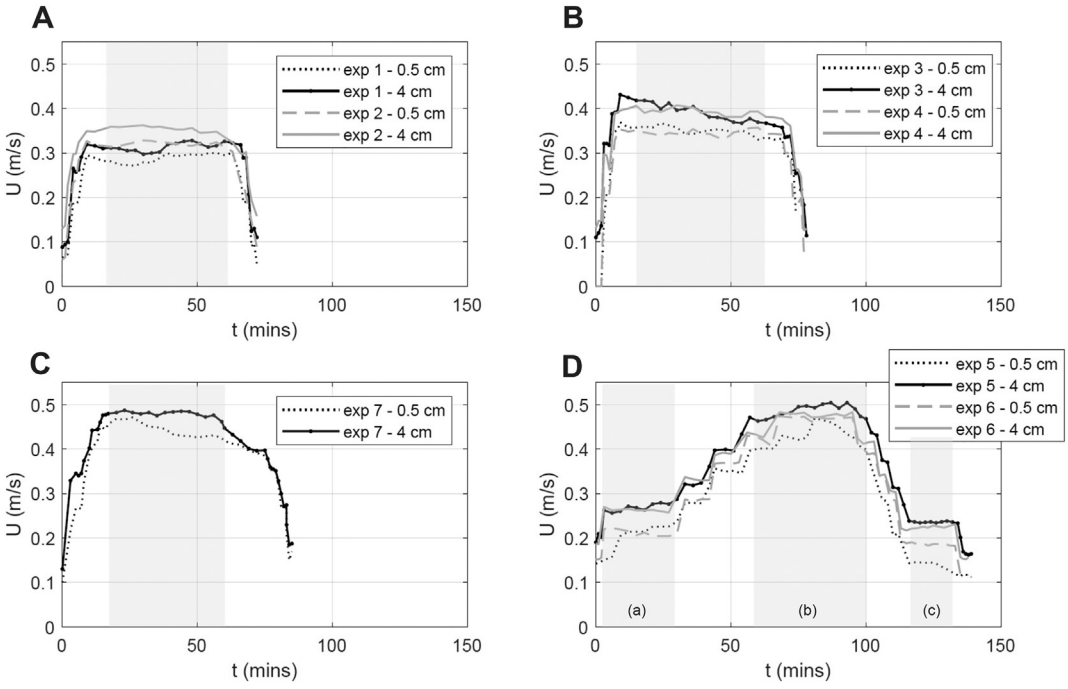

Fig. 3. Velocity time series, with velocity (U) in m s^{-1} and time (t) in minutes, for all experiments showing average velocities varied between 0.30 and 0.50 m s^{-1}. Dotted lines indicate the flow meter close to the bed (0.5 cm), solid lines are the velocity measurements 4 cm above the bed. Grey shaded areas indicate the intervals of constant velocity over which the average flow velocity was calculated, see Table 1.

measurement spacing with a ~10 μm^3 interaction volume. The measured chemistry of each point (pixel) is compared to a library and assigned to a specific mineral phase, resulting in a quantitative 2D mineralogical representation for each sample. Detailed mineral maps were created and data interpretation was performed using the iDiscover software. Mineral association tables, reporting the number of pixels of each mineral phase in contact with the other mineral phases, were used to quantify the clay coat cover for each sample (Table 2):

$$clay\ coat\ cover = \frac{qtz_{clays}}{(qtz_{clays} + qtz_{porosity})}, \quad (3)$$

where qtz_{clays} is the sum of the illite, kaolinite and chlorite pixels that are in contact with quartz pixels and $qtz_{porosity}$ is the total of quartz pixels in

Table 2
Data collected from BSEM and SEM-EDS data analysis comparing the average, initial clay coat characteristics before the experiments to the clay coat characteristics after each experiment. The table reports the duration of each experiment, the maximum velocity at 4 cm above the bed (U_{max}), clay coat cover (Eq. 3) and clay coat thickness (mean, standard deviation, minimum, maximum), as well as the parameters needed to evaluate the amount of clay minerals available to form clay coats (Eqs. 4 and 5): the total number of pixels analysed in the SEM-EDS analysis (pxl_{total}), the total number of pixels of each clay mineral (e.g. ilt_{pxl}), the total number of pixels of each clay mineral that exceeds the cut-off value (e.g. $ilt_{pxl>24\mu m}$), the total of each clay mineral available (e.g. ilt_{total}), the total of each clay mineral available to form coats (e.g. ilt_{coat}), and the percentage of each clay mineral available to form coats (e.g. illite % to coat).

Experiment	before transport (avg.)	1	2	3	4	5	6	7
Duration (min)	N/A	73	73	79	79	140	139	89
U_{max} (at 4 cm) (m s^{-1}))	N/A	0.33	0.36	0.42	0.41	0.50	0.48	0.49
Clay coat cover (%)	41.6	24.0	20.3	20.8	21.6	21.3	20.0	25.1
Clay coat thickness (mean; μm)	3.8	2.3	1.9	2.2	2.7	2.2	2.1	2.1
Clay coat thickness (σ) deviation	2.1	1.6	1.1	1.2	1.3	1.3	1.3	1.0
Clay coat thickness (min.; μm)	1.1	0.8	0.5	0.7	0.9	0.7	0.7	0.7
Clay coat thickness (max.; μm)	11.4	10.9	8.0	8.0	7.1	8.9	6.9	4.6
pxl_{total}	994,647.2	1,092,786.0	1,213,587.0	756,235.0	711,326.0	678,269.0	1,015,094.0	574,475.0
ilt_{pxl}	137,375.4	66,508.0	66,638.0	34,564.0	33,985.0	40,015.0	47,322.0	41,673.0
ilt_{total} (area%)	13.8	6.1	5.5	4.6	4.8	5.9	4.7	7.3
$ilt_{pxl>24\mu m}$	11,004.8	2347.0	3299.0	1571.0	1559.0	2156.0	1715.0	2260.0
ilt_{coat} (area%)	13.0	5.9	5.3	4.4	4.6	5.7	4.5	7.0
illite % to coat (%)	93.9	97.5	95.9	96.8	96.4	96.3	97.3	96.0
kao_{pxl}	15,762.6	7301.0	8934.0	8730.0	4688.0	6271.0	8269.0	6476.0
kao_{total} (area%)	1.6	0.7	0.7	1.2	0.7	0.9	0.8	1.1
$kao_{pxl>16\mu m}$	1474.0	1467.0	2057.0	1081.0	780.0	1785.0	2635.0	517.0
kao_{coat} (area%)	1.5	0.5	0.6	1.0	0.6	0.7	0.6	1.1
kaolinite % to coat (%)	92.5	80.8	77.7	88.8	84.2	72.8	68.8	93.4
chl_{pxl}	19,333.0	14,637.0	13,203.0	12,426.0	9233.0	13,699.0	10,166.0	11,633.0
chl_{total} (area%)	1.9	1.3	1.1	1.6	1.3	2.0	1.0	2.0
$chl_{pxl>16\mu m}$	7858.0	7671.0	5917.0	7708.0	5010.0	7984.0	4827.0	5984.0
chl_{coat} (area%)	1.2	0.6	0.6	0.6	0.6	0.9	0.5	1.0
chlorite % to coat (%)	60.6	48.1	55.7	38.5	46.2	42.5	53.0	49.3

contact with porosity. To quantify and evaluate how much of the clay minerals were available to form coats in each sample, monomineralic clay particles or aggregates with a long axis greater than a user-defined size were assumed to be lithic fragments, clay flocs, or intraclasts rather than clay coat components (Wooldridge et al., 2019a). The long axis cut-off values used in this study, >24 μm for illite and > 16 μm for chlorite and kaolinite, were determined after detailed visual comparison of sample mineral maps with different cut-off values. Using illite as an example, the total amount of clay and amount of clay available to form coats (Table 2) were calculated as follows:

$$ilt_{total} = \frac{ilt_{pxl}}{pxl_{total}} \times 100, \quad (4)$$

where ilt_{total} is the total illite in the sample (in area%), ilt_{pxl} is the total number of illite pixels measured, and pxl_{total} is the total number of pixels analysed in the SEM-EDS analysis.

$$ilt_{coat} = \frac{(ilt_{pxl} - ilt_{pxl>24}\mu m)}{pxl_{total} - (ilt_{pxl>24}\mu m + kao_{pxl>16}\mu m + chl_{pxl>16}\mu m)} \times 100, \quad (5)$$

where ilt_{coat} is the total illite available to form clay coats, $ilt_{pxl>24\mu m}$ is the total number of illite pixels that exceed the 24 μm cut-off value, and $kao_{pxl>16\mu m}$ and $chl_{pxl>16\mu m}$ are the total number of kaolinite and chlorite pixels that exceed the 16 μm cut-off value.

Approximately 150 BSEM images were analysed to compare changes in clay coat thickness, cover and continuity before and after the sediment transport experiments. For each sample the thickness of 100 clay coats was measured perpendicular to the grain surface, using randomly selected BSEM images and ImageJ software (v1.48). Additionally, Al-K_α and Fe-K_α element distribution maps were created with the BSE microscope software to visualise the continuity and mineralogy of the clay coats at high resolution.

4. Results

4.1. Flow characteristics

Velocity time series for each experiment are shown in Fig. 3. The curves display the step-wise acceleration and deceleration at the start and end of each experiment used to prevent sudden changes in flow characteristics. The maximum velocity ranged from 0.30 m s^{-1} (experiment 1 and 2, Fig. 3A) to 0.50 m s^{-1} (experiments 5–7, Fig. 3). Velocity measurements were lower near the bed than at 4 cm in the flow, but both flow meters recorded the same trends in the flow velocity (Table 1). Based on their Froude and Reynolds numbers (Eqs. 1 and 2) the flows are subcritical ($Fr < 1$) and turbulent ($Re > 2000$).

Sediment was transported both as suspended load and bedload. Clasts up to 4 mm in diameter were observed to slide and roll on the bed surface. When the flow velocity exceeded 0.30 m s^{-1}, sediment accumulated in a ripple-like bedform downstream of the paddle wheel (Fig. 2B). The maximum height of this bedform was 6 mm; this was slightly lower (approx. 4 mm) in experiments with higher average flow velocities (experiments 5–7). The bedform did not migrate during the experiments, however some of the accumulated sediment was reworked by sliding and rolling and/or re-incorporated into the suspended load.

4.2. Mineralogy and grain-coating clays

4.2.1. Before sediment transport

The BSEM and SEM-EDS data show that the initial sediment was very fine to fine, moderately sorted sand, containing angular to sub-angular grains (Figs. 4, 5A-C, 6A-C). The most abundant minerals in the samples prior to transport are quartz (50%), feldspars (13%) and clay minerals (17.3%), which are dominated by illite (13.8%) and small quantities of chlorite (1.9%) and kaolinite (1.6%) (Fig. 5A-C). Some calcite (4.3%) and dolomite (2.4%) are also present. Bulk SEM-EDS mineralogy of the samples is consistent, with generally <0.6% difference (standard deviation) in mineral abundance between all analysed samples, while quartz shows a slightly larger variation of 1.9%.

The clay minerals illite, kaolinite and chlorite are present as, or part of, lithic grains and clay coats (Figs. 4, 5A-C, 6A-C). Monomineralic lithic grains consist mainly of chlorite and kaolinite (Fig. 5C), while all three clay minerals can be present in lithic grains that are composed of multiple minerals (Fig. 5I, L). The detrital clay coats are present in all three principle morphologies recognised by Wooldridge et al. (2017b): ridges, bridges and clumps (Figs. 4, 6A-C). The coats have a mixed mineralogy, predominantly composed of illite with minor kaolinite and chlorite (Figs. 5B-C, 6B-C), which is consistent with the element maps of Al-K_α and Fe-K_α shown in Figs. 7A-C (Worden and Morad, 2003). Prior to sediment transport, the detrital coats are abundant on the surfaces of framework grains (Fig. 4), with an estimated clay coat cover of 41.6% (Eq. 3, Table 2). The thickness of the coats is on average 3.8 μm, ranging between 1.1 and 11.4 μm (Table 2), with thicker coats on grain surfaces that are irregular and have indentations (e.g., yellow arrows on Fig. 4). Clay bridges between framework grains are common

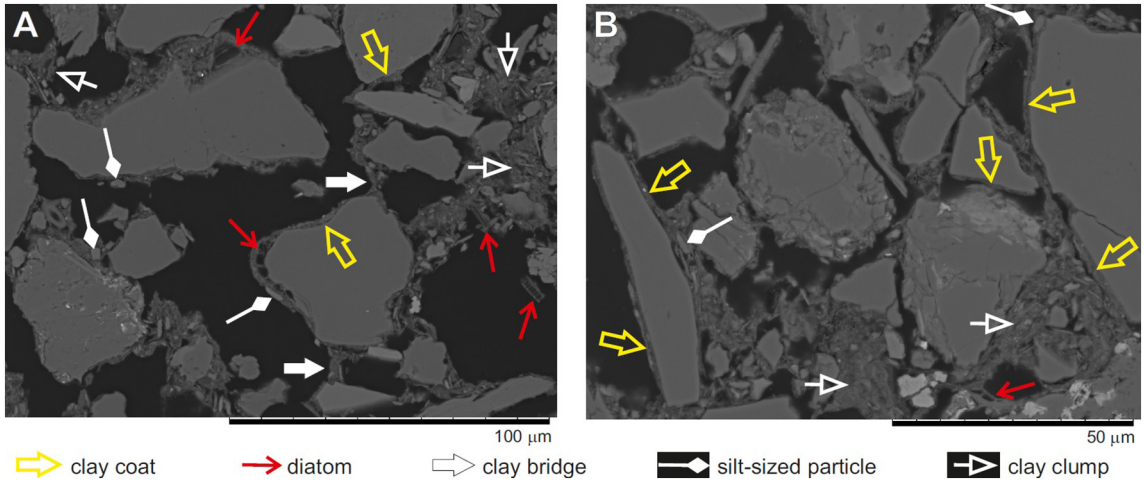

Fig. 4. Detailed BSEM images of sediment samples taken before experiments 5 (A) and 6 (B) showcasing the different textures of the clay coats, specifically highlighting clay bridges, clay clumps, diatoms and silt-sized particles within the coats.

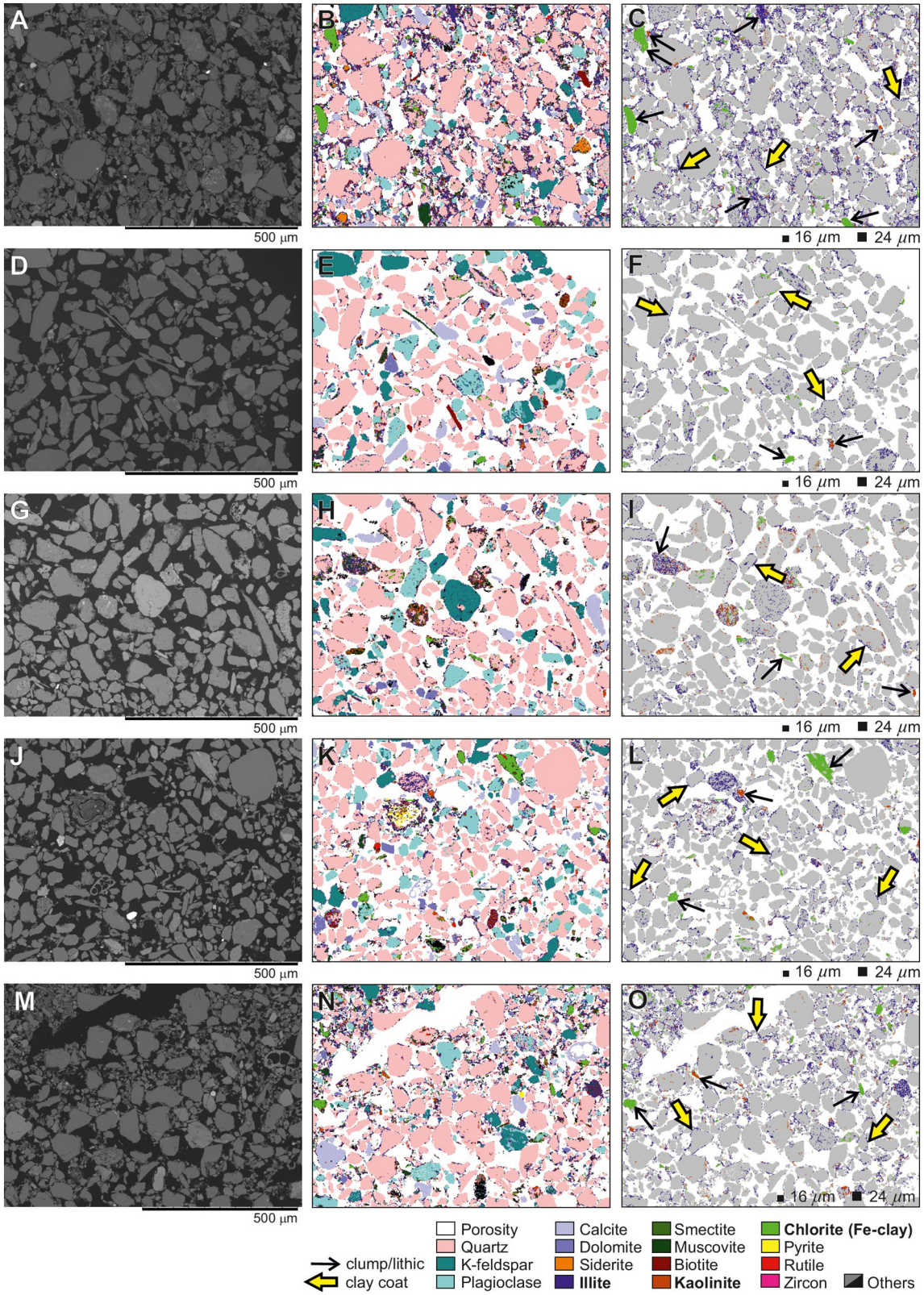

Fig. 5. Overview BSEM images (left) with matched SEM-EDS maps showing all minerals (middle) and maps coloured only for illite, chlorite and kaolinite (right) from sediment samples taken before and after the experiments. (A-C) initial sediment prior to experiment 6. (D-F) sediment after experiment 1 ($\bar{U} = 0.29$ m s^{-1}). (G-I) sediment after experiment 3 ($\bar{U} = 0.35$ m s^{-1}). (J-L) sediment after experiment 5 (varied $\bar{U}$, see Table 1). (M-O) sediment after experiment 7 ($\bar{U} = 0.44$ m s^{-1}). The sets of images show a progressive reduction in the amount of clay minerals available to coat the grains (see also Table 2), noted by the reduction in fines in the BSEM images paired with the reduction in blue (illite), bright green (chlorite) and brown (kaolinite) pixels in the SEM-EDS maps. The selectively coloured mineral maps highlight examples of clay coats (yellow arrows) and clump/lithic clasts (black arrows; >24 μm for illite, and 16 μm for kaolinite and chlorite). (For interpretation of the references to colour in this figure legend, the reader is referred to the web version of this article.)

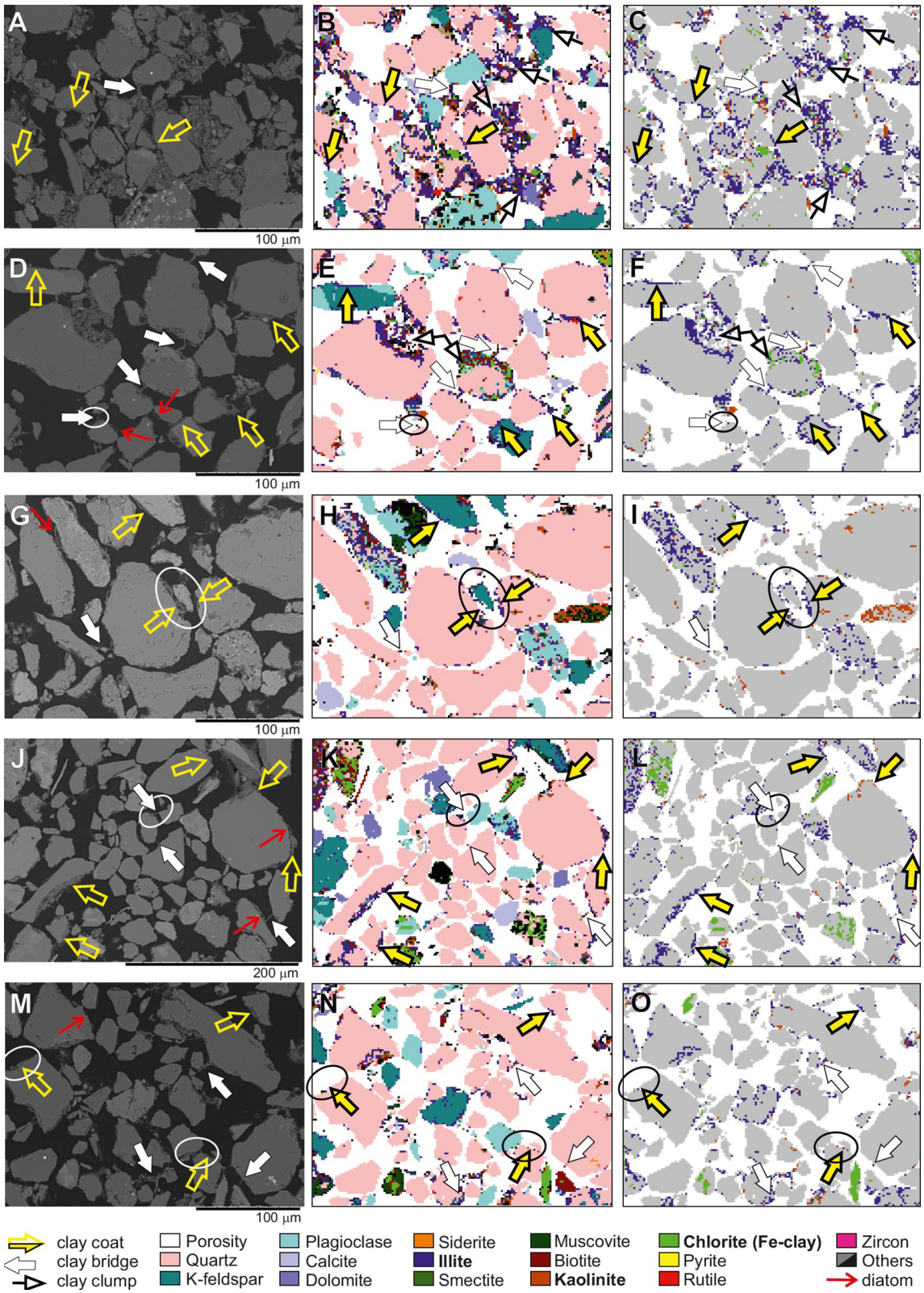

Fig. 6. Detailed BSEM and matched SEM-EDS maps, corresponding to the same experiments shown in Fig. 4, highlighting clay mineral and grain coat characteristics before and after sediment transport. (A-C) initial sediment prior to experiment 6 contains abundant clay minerals as coats and clumps. (D-F) sediment after experiment 1 ($\bar{U} = 0.29$ m s^{-1}) contains thin and discontinuous coats which are thicker on grain indentations, thin clay bridges, and diatoms as part of the coat. (G-I) sediment after experiment 3 ($\bar{U} = 0.35$ m s^{-1}), shows thin clay bridges and clay coats. (J-L) sediment after experiment 5 (varied $\bar{U}$, see Table 1) contains abundant thin bridges as well as thin, discontinuous coats that are thicker in grain indentations. (M-O) sediment after experiment 7 ($\bar{U} = 0.44$ m s^{-1}) shows a similar trend to the other experiments, despite the higher flow velocities. Circled areas indicate examples of where the SEM-EDS analysis did not record all grain coats. (For interpretation of the references to colour in this figure legend, the reader is referred to the web version of this article.)

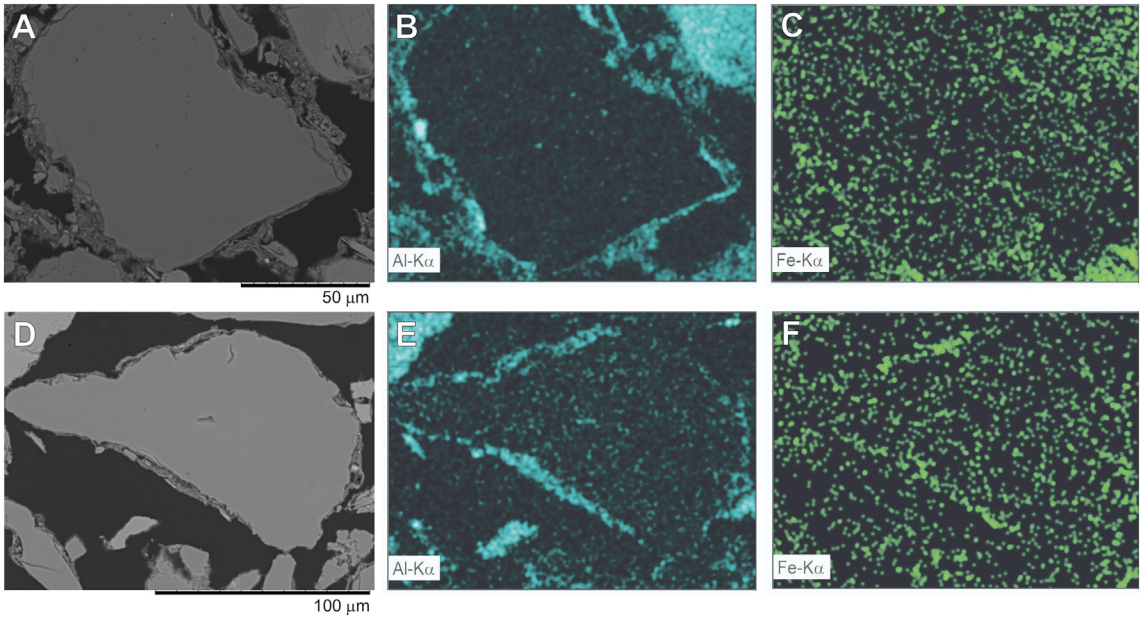

Fig. 7. Detailed BSEM images of grain coats with element maps for Al-K_α and Fe-K_α, corresponding to illite, kaolinite and chlorite clays. (A-C) show the initial sediment in experiment 6. (D-F) are images from experiment 4 after sediment transport ($\bar{U} = 0.35$ m s^{-1}, Table 1). The element maps, particularly Al_α-K_α, show continuous grain-coats prior to sediment transport (e.g., B) which are preserved during sediment transport, mainly in grain indentations (E).

(white arrows on Figs. 4A, 6A-C). The coats contain silt-sized particles and diatoms (Fig. 4), which can form ridge-like morphologies that result in thicker coats (Fig. 4A).

4.2.2. After sediment transport

The largest proportional changes in mineralogy after sediment transport are seen in quartz, which increases to 63%, and clay minerals which are reduced to 7.9% of the sample (Fig. 5D-O).

Table 2 shows a detailed breakdown of the changes in clay mineral content of the samples, comparing each sample to the average initial mineralogy before the transport experiments. On average, the total illite was reduced to 5.5%, whereas kaolinite and chlorite were reduced to 0.9% and 1.5% respectively (Table 2). This translates into an average 60% reduction in illite, a 45% reduction in kaolinite and a 23% reduction in chlorite, although two samples (experiments 5 and 7) actually contain a very similar amount of chlorite compared to the pre-transport average (Table 2). Chloritic and kaolinitic lithic grains are still present (e.g. Fig. 5F, L, O), but clumps are rare (Figs. 5, 6). The estimated amount of clay minerals that are available to coat is also reduced for both kaolinite (from 92.5% to 81% on average) and chlorite (from 60.6% to 47.6%; Table 2). For illite however, the amount available to coat after the experiments has increased from 93.9% to 96.6% (Table 2).

The main changes in grain coat characteristics after the transport experiments are an overall reduction of their coverage and thickness (Fig. 6, Table 2). The clay coat cover is reduced to ~22% on average (compared to the initial 41.6%; Table 2), which marks a reduction of 47% compared to the samples before transport. Where present, the coats are thinner (2.2 μm on average, compared to the initial 3.8 μm), partial and irregular, and mostly preserved in and around grain indentations (Figs. 6D-O, 7D). Fig. 6D-O also shows that the clay bridges are thinner and less common, but diatoms are still present in the samples.

The changes described above were observed in samples of all experiments, both BSEM and SEM-EDS analyses did not reveal distinct differences between the experiments performed at different flow velocities. However, the BSEM images (Fig. 6D, G, J, M) and the element distribution maps (Fig. 7) show continuous coats around the framework grains and clay bridges that were not always recorded by the SEM-EDS analysis (circled areas on Fig. 6D-O).

5. Discussion

5.1. Clay coat characteristics

The mineralogical and textural properties of the sediment samples prior to transport are characteristic of the Ravenglass estuary mixed sand- and mud-flat sediments and correspond with observations discussed by Wooldridge et al. (2017b) and Daneshvar and Worden (2018). The extensive coverage (>40%) and thickness (~3.8 μm) of the clay coats and bridges (Figs. 5A-C, 6A-C) support the interpretation that they formed through a combination of infiltration, bioturbation processes, and the presence of biofilms on sand grains (Matlack et al., 1989; Needham et al., 2005; Worden et al., 2006; Wooldridge et al., 2017a, 2018). Infiltration likely created the ridge or cutan-like coatings with clay minerals parallel to the grain surface (Figs. 4, 7A; Wilson, 1992; Wooldridge et al., 2017b; Molenaar and Felder, 2018). The bioturbation processes and biofilms introduced bio-glue, e.g., mucous produced by lugworms (Needham et al., 2005) and EPS (Wooldridge et al., 2017a), that attached clay minerals to grain surfaces and is most likely responsible for the thicker, clump-like coatings (Figs. 4, 7A).

After sediment transport a marked reduction in the total clay mineral content was evident, particularly in amount of clumps (Figs. 5, 6) and total illite (Table 2; Fig. 8). The greater reduction in illite can be attributed to the break-up and winnowing of the clay clumps, in which illite is more abundant (Figs. 5B-C, 6B-C), whereas chlorite and kaolinite occur more often in lithic grains which are preserved during transport (Figs. 5, 6). Apart from lithic grains, some grain coats and clay bridges were still present in the samples (Figs. 5 and 6), suggesting at least part of the coat can survive prolonged sediment transport processes. Diatoms were still attached to, and part of, the partial coats after sediment transport (Fig. 6D, G, J, M), which implies they might have an influence on overall clay coat thickness and stability.

The 41% reduction in clay coat thickness and 47% reduction in clay coat cover after sediment transport, but not complete removal of the coats (Fig. 6D-O; Table 2; Fig. 8), supports the suggestions of Wilson (1992) that mild reworking allows for preservation of clay coats. Clay bridges are thinner and less common in the samples after the experiments, however if the sediment transport was extended as well as abrasive they are not expected to survive (Wilson, 1992; Figs. 6, 8). An

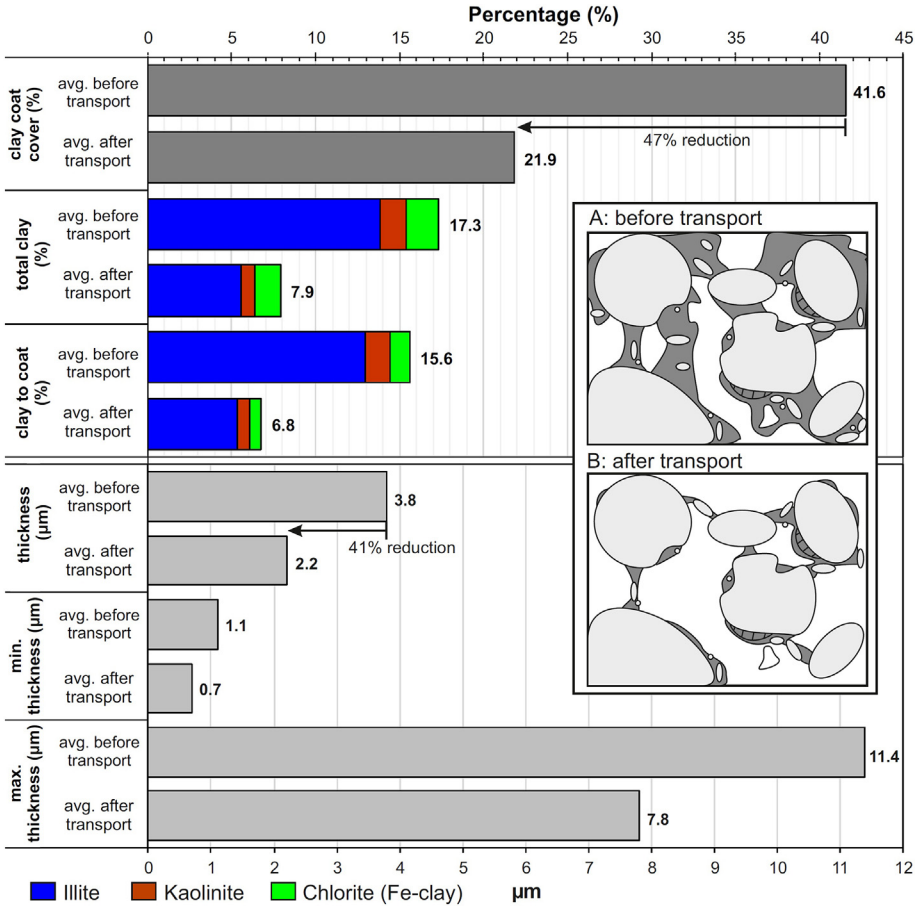

Fig. 8. Summary diagram demonstrating the changes observed in the clay coat cover, total clay mineral content, clay minerals available to coat, and changes in the clay coat thickness before and after the sediment transport experiments. Insets (A) and (B) represent schematic 2D views of a sediment sample before and after transport showing a reduction in clay coat thickness and cover (framework grains in light grey, clay coats in dark grey).

alternative explanation is that these bridges formed through infiltration (e.g., Matlack et al., 1989; Moraes and De Ros, 1990) during settling of the clay minerals prior to draining the flume tank after the experiments. However it is unlikely the 60-min time period is sufficient to allow the formation of bridges and (partial) coats. There is also no repeat wetting by clay-rich water and drying which has been suggested to form thicker bridges and complete grain coats (Ajdukiewicz and Larese, 2012).

Fig. 6D-O highlight areas on the BSEM images where clay minerals are present, but the SEM-EDS analysis of the same area of the sample did not record them. This is because the very fine clay particles and thin coatings are smaller than the SEM-EDS interaction volume and are therefore included in the mineralogy of surrounding mineral phases. This is a key limitation of the SEM-EDS technique that means that the amount of clay minerals estimated to coat the grains as well as the amount that is available to coat (Table 2; Fig. 8) is probably underestimated.

5.2. Flow dynamics

Clay-rich sediment has the potential to modify fluid flow properties during sediment transport processes. In a series of flume experiments Baas and Best (2008) and Baas et al. (2009) showed that, at low flow velocities (<0.5 m s^{-1}), a clay concentration as low as 0.04% is enough to change flow behaviour. The non-dimensional diagram of flow phases they present (see Fig. 17 in Baas et al., 2009) is not directly applicable to the flows in this study because it was based on single clay flows (kaolinite) with a greater flow depth (0.13–0.16 m). Tentative comparison of Froude and Reynolds numbers and assuming a low clay concentration in the flow (<2 vol%, based on video and photo data), pinpoints turbulence-enhanced transitional flow (TETF), and lower transitional plug flow (LTPF) at low flow velocities (see Fig. 15 in Baas et al., 2009), as the most likely flow phases in the experiments. The small velocity fluctuations visible during periods of constant flow velocity (Fig. 3A-C) may be related to the turbulence near the bed (at 0.5 cm) and in free-shear layers (at 4 cm), although the velocity measurements shown here are at lower resolution than those reported by Baas et al. (2009). The LTPF and TETF flow behaviour is further evidenced by sediment transport processes observed on the lee side of the bedform that formed during the experiments (Fig. 9). Due to the TETF flow conditions, flow separation is enhanced (Baas and Best, 2008) and able to suspend grains back into the flow.

The TETF flow phase is characterised by enhanced turbulence (Baas and Best, 2008; Baas et al., 2009, 2011). It is likely that turbulence will have the largest impact on grain-coating clay abrasion as it facilitates grain movement (e.g. rolling and saltating) and grain-to-grain interactions which could cause abrasion of the coats. The similarity in flow properties between experiments could explain the comparable characteristics of all samples taken after sediment transport (Figs. 4, 6).

5.3. Entrapment within bedforms

Sediment movement was evident in all experiments with flow velocities >0.20 m s^{-1} and it consistently created a bedform downstream of the paddle wheel (Figs. 2B, 9A). Flow separation and enhanced turbulence near the bedform are likely responsible for winnowing the clay-sized sediment fraction out of the sediment, particularly the clay clumps and therefore illite (Table 2; Figs. 6, 8). Experiments by Baas et al. (2013)

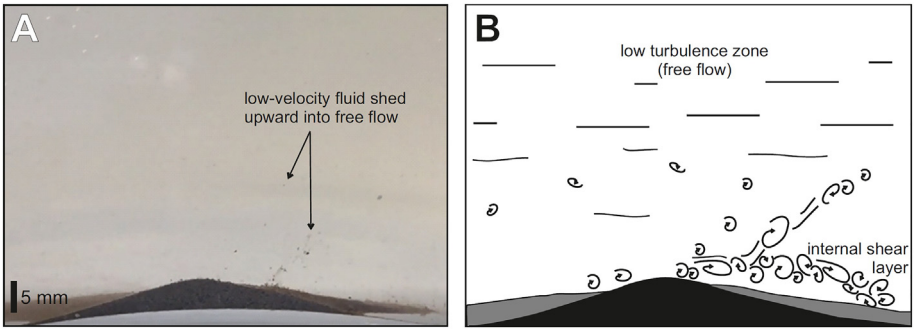

Fig. 9. (A) shows the bedform during experiment 4. (B) displays the interpreted flow dynamics on the lee side of the bedform in turbulence enhanced transitional flow conditions (based on the conceptual model of Baas and Best, 2008). This corresponds to lower transitional plug flow (LTPF) and turbulence-enhanced transitional flow (TETF) conditions of Baas et al. (2009). Indicative of the flow conditions are the packages of low-velocity fluid shed upward from the internal shear layer. These packages are able to carry grains back into the flow allowing for continued transport.

showed similar effective winnowing of sand-mud mixtures that resulted in cleaner sand current ripples.

All sediment samples after the experiments were taken from the downstream bedform to ensure a minimum transport distance of approx. 1.5 m. Due to the accumulation of the sediment, the bedform could act as a trap for grains with 'left-over' (partial) clay coats and preserve these coats in cases where the grains are not reworked. Ajdukiewicz et al. (2010) presented a similar interpretation for abraded, detrital grain-coating clays in the aeolian Norphlet Formation (Gulf of Mexico).

5.4. Proposed implications for reservoir quality

The changes observed in the detrital grain-coating clays as a result of sediment transport can impact their effectiveness as precursor coats and affect final reservoir quality after burial, compaction, and cementation of the estuarine sands.

The reduction of clay coat coverage after sediment transport (Table 2; Fig. 8) could have a negative effect on final reservoir quality by removing the barrier for quartz cementation. However, recrystallisation of discontinuous precursor detrital coats can still lead to continuous diagenetic coats like those found in deeply buried sandstone reservoirs (Aagaard et al., 2000; Wooldridge et al., 2017b). These diagenetic coats can be effective quartz cement growth inhibitors even if they are only a few micrometres thick (Chen et al., 2011; Churchill et al., 2017; Skarpeid et al., 2018; Table 2). Therefore, the potential of the detrital grain-coating clays to prevent quartz cementation themselves (e.g. inherited cutans of Molenaar and Felder, 2018) or act as precursors of diagenetic grain-coating clay minerals will still be present despite the reduction of the coat coverage, unless the coat is completely removed or the recrystallisation results in thick grain-rimming illite or kaolinite (Waldmann and Gaupp, 2016; Molenaar and Felder, 2018). Moreover, the winnowing of the clay fraction (clay clumps) will further enhance potential reservoir quality as this process would result in cleaner clay-coated sands.

A positive effect on final reservoir quality might be linked to the presence of diatoms in the sediment (Figs. 4, 6). Diatoms produce biofilms which increase the cohesion of the sediment, making it more difficult to erode (Tolhurst et al., 2000; Grabowski et al., 2011; Baas et al., 2013; Wooldridge et al., 2017a). This could therefore protect detrital grain-coating clays from abrasion during sediment transport, which in turn leads to thicker remnant coats as potential precursors for diagenetic coatings.

Partial abrasion of the coats in the finer-grained sediments could also have a positive effect by reducing the ultimate diagenetic coat thickness in deeply buried sandstones. Conversely, preserving part of the detrital coat in the fine-grained sediments could negatively impact final reservoir quality by reducing pore throat size. This impact is greater in fine sands compared to medium and coarse sands when these are buried and enter the mesodiagenetic realm (2500 m, 80–90 °C) (Bloch et al., 2002).

If the detrital clay coats can be preserved by entrapment in bedforms, a similar process might happen in submarine gravity flows where grain collisions would likely have less impact compared to other transport processes (Bloch et al., 2002). This could explain the occurrence of grain coats in turbidite reservoir sandstones (Sullivan et al., 1999; Loizou et al., 2006). But since submarine gravity flow dynamics and flow-bed interaction varies considerably with different flow and bed properties (Talling et al., 2012; Verhagen et al., 2013), determining the preservation potential of grain-coating clays within these flows is not straightforward.

One of the pre-requisites to form effective porosity-preserving, chloritic grain coats is the presence of Fe- and Al-rich precursors such as detrital Fe-phyllosilicates, neoformed Fe-clay (e.g., berthierine), Fe-hydroxides, or dissolution of lithic chlorite fragments (Ehrenberg, 1993; Worden and Morad, 2003; Dowey et al., 2012) (Figs. 5, 6). The mineralogical composition of the samples after sediment transport showed a slight increase in the proportions of chlorite (Fe-rich precursor phyllosilicate) and kaolinite (Al-rich) with respect to illite (Table 2). The element distribution images also highlight that the transported grain-coating clay minerals are Al- and Fe-rich (Fig. 7). The final mineralogy is therefore more likely to develop diagenetic grain-coating clays with a chloritic composition, the most effective coats for preserving reservoir quality in buried sandstones.

6. Conclusions

(1) Sediment transport processes caused a distinct reduction in the thickness (41%, from 3.8 μm to ~2.2 μm) and coverage (47%, from 41.6% to ~22%) of the detrital clay coats, including a reduction in clay clumps and thickness of the detrital clay bridges between the grains.
(2) Partial clay coats are preserved during prolonged (60 min) turbulent, open-channel flow conditions with velocities up to at least 0.5 m s^{-1}.
(3) The preservation potential of the detrital clay coats can be linked to the initial coverage and thickness of the coats, turbulence properties of the flow, and entrapment in sedimentary bedforms.
(4) The presence of diatoms in the sediment implies that biofilms may also play a role in the preservation of detrital clay coats.
(5) When preserved, the detrital grain-coating clays can act as precursors for diagenetic grain-coating clay minerals and positively impact final reservoir quality. Fe- and Al-rich coats in particular have the potential to form grain-coating chlorite during burial and diagenesis of the estuarine sands.

Acknowledgements

This work was carried out as part of a dissertation project entitled *Stability of detrital grain-coating clays during sediment transport* for the Petroleum Reservoir Geoscience MSc at the University of Liverpool

(UK). Adriana Crisóstomo-Figueroa received funding to undertake the MSc from CONACyT-SENER Hidrocarburos 2016-2017 3er Periodo. The authors wish to thank FEI for the loan of the QEMSCAN® system, as well as Prof. Jasper Knight and an anonymous reviewer whose comments helped to markedly improve this manuscript.

References

Aagaard, P., Jahren, J.S., Harstad, A.O., Nilsen, O., Ramm, M., 2000. Formation of grain-coating chlorite in sandstones. Laboratory synthesized vs. natural occurrences. Clay Miner. 35, 261–269.

Ajdukiewicz, J.M., Larese, R.E., 2012. How clay grain coats inhibit quartz cement and preserve porosity in deeply buried sandstones: Observations and experiments. Am. Assoc. Pet. Geol. Bull. 96, 2091–2119.

Ajdukiewicz, J.M., Nicholson, P.H., Esch, W.L., 2010. Prediction of deep reservoir quality using early diagenetic process models in the Jurassic Norphlet Formation, Gulf of Mexico. Am. Assoc. Pet. Geol. Bull. 94, 1189–1227.

Amos, C.L., Brylinsky, M., Sutherland, T.F., O'Brien, D., Lee, S., Cramp, A., 1998. The stability of a mudflat in the Humber estuary, South Yorkshire, UK In: Black, K.S., Paterson, D. M., Cramp, A. (Eds.), Sedimentary Processes in the Intertidal Zone. Geol. Soc. Lond., Spec. Publ. 139, pp. 25–43.

Anjos, S.M.C., De Ros, L.F., Silva, C.M.A., 2003. Chlorite Authigenesis and Porosity Preservation in the Upper cretaceous Marine Sandstones of the Santos Basin, Offshore Eastern Brazil. In: Worden, R.H., Morad, S. (Eds.), Clay Mineral Cements in Sandstones. International Association of Sedimentologists Special Publication 34, pp. 291–316.

Baas, J.H., Best, J.L., 2002. Turbulence modulation in clay-rich sediment-laden flows and some implications for sediment deposition. J. Sediment. Res. 72, 336–340.

Baas, J.H., Best, J.L., 2008. The dynamics of turbulent, transitional and laminar clay-laden flow over a fixed current ripple. Sedimentology 55, 635–666.

Baas, J.H., Best, J.L., Peakall, J., Wang, M., 2009. A Phase Diagram for Turbulent, Transitional, and Laminar Clay Suspension Flows. Journal of Sedimentary Research 79, 162–183.

Baas, J.H., Best, J.L., Peakall, J., 2011. Depositional processes, bedform development and hybrid bed formation in rapidly decelerated cohesive (mud-sand) sediment flows. Sedimentology 58, 1953–1987.

Baas, J.H., Davies, A.G., Malarkey, J., 2013. Bedform development in mixed sand-mud: the contrasting role of cohesive forces in flow and bed. Geomorphology 182, 19–32.

Billault, V., Beaufort, D., Baronnet, A., Lacharpagne, J.C., 2003. A nanopetrographic and textural study of grain-coating chlorites in sandstone reservoirs. Clay Miner. 38, 315–328.

Bloch, S., Lander, R.H., Bonnell, L., 2002. Anomalously high porosity and permeability in deeply buried sandstone reservoirs: Origin and predictability. Am. Assoc. Pet. Geol. Bull. 86, 301–328.

Bousher, A., 1999. RESTRAT - Ravenglass Estuary: Basic Characteristics and Evaluation of Restoration Options. Technical Report 4. Ltd, Westlakes Scientific Consulting.

Brown, J.M., Davies, A.G., 2010. Flood/ebb tidal asymmetry in a shallow sandy estuary and the impact on net sand transport. Geomorphology 114, 431–439.

Cartigny, M.J., Ventra, D., Postma, G., van Den Berg, J.H., 2014. Morphodynamics and sedimentary structures of bedforms under supercritical-flow conditions: New insights from flume experiments. Sedimentology 61, 712–748.

Chen, G., Du, G., Zhang, G., Wang, Q., Lv, C., Chen, J., 2011. Chlorite cement and its effect on the reservoir quality of sandstones from the Panyu low-uplift, Pearl River Mouth Basin. Petroleum Science 8, 143–150. Doi:10. 1007/s12182-011-0127-z.

Christie, M., Dyer, K., 1998. Measurements of the turbid tidal edge over the Skeffling mudflats In: Black, K., Paterson, D.M., Cramp, A. (Eds.), Sedimentary Processes in the Intertidal Zone. Geol. Soc. Lond., Spec. Publ. 139, pp. 45–55.

Churchill, J.M., Poole, M.T., Skarpeid, S.S., Wakefield, M.I., 2017. Stratigraphic architecture of the Knarr Field, Norwegian North Sea: Sedimentology and biostratigraphy of an evolving tide- to wave-dominated shoreline system. In: Hampson, G.J., Reynolds, A. D., Kostic, B., Wells, M.R. (Eds.), Sedimentology of Paralic Reservoirs: Recent Advances. Geological Society, London, Special Publications 444, pp. 35–58.

Coussot, P., 1997. Mudflow Rheology and Dynamics. International Association for Hydraulic Research Monograph Series. A.A. Balkema, Rotterdam.

Daneshvar, E., 2015. Dissolved iron behaviour in the Ravenglass Estuary waters, an implication on the early diagenesis. Universal Journal of Geoscience 3, 1–12.

Daneshvar, E., Worden, R.H., 2018. Feldspar alteration and Fe minerals: Origin, distribution and implications for sandstone reservoir quality in estuarine sediments. In: Armitage, P.J., Butcher, A.R., Churchill, J.M., Csoma, A.E., Hollis, C., Lander, R.H., Omma, J.E., Worden, R.H. (Eds.), Reservoir Quality of Clatic and Carbonate Rocks. Geological Society, London, Special Publications 435, pp. 123–139.

Dowey, P.J., Hodgson, D.M., Worden, R.H., 2012. Pre-requisites, processes, and prediction of chlorite grain coatings in petroleum reservoirs: a review of subsurface examples. Mar. Pet. Geol. 32, 63–75.

Dowey, P.J., Worden, R.H., Utley, J., Hodgson, D.M., 2017. Sedimentary controls on modern sand grain coat formation. Sediment. Geol. 353, 46–63.

Ehrenberg, S.N., 1993. Preservation of anomalously high porosity in deeply buried sandstones by grain-coating chlorite: examples from the Norwegian Continental Shelf. Am. Assoc. Pet. Geol. Bull. 77, 1260–1286.

Grabowski, R.C., Droppo, I.G., Wharton, G., 2011. Erodibility of cohesive sediment: the importance of sediment properties. Earth Sci. Rev. 105, 101–120.

Griffiths, J., Worden, R.H., Wooldridge, L.J., Utley, J.E., Duller, R.A., 2018. Clay coats, clay minerals, pyrite and estuarine facies: modern shallow-core analogue for ancient deeply-buried sandstones. J. Sediment. Res. 88, 1205–1237.

Griffiths, J., Worden, R.H., Wooldridge, L.J., Utley, J.E., Duller, R.A., 2019. Compositional variation in modern estuarine sands: predicting major controls on sandstone reservoir quality. Am. Assoc. Pet. Geol. Bull. 4, 797–833.

Griffiths, J., Worden, R.H., Wooldridge, L.J., Utley, J.E., Duller, R.A., Edge, R.L., 2019b. Estuarine clay mineral distribution: Modern analogue for ancient sandstone reservoir quality prediction. Sedimentology 66, 2011–2047.

G.U.N.T. Hamburg, 2018. HM166 Fundamentals of sediment transport data sheet. https://www.gunt.de/images/datasheet/765/HM-166-Fundamentals-of-sediment-transport-gunt-765-pdf_1_en-GB.pdf, Accessed date: 11 March 2020.

Heald, M.T., Larese, R.E., 1974. Influence of coatings on quartz cementation. J. Sediment. Res. 44, 1269–1274.

Houseknecht, D.W., Ross Jr., L.M., 1992. Clay Minerals in Atokan Deep-Water Sandstone Facies, Arkoma Basin: Origins and Influence on Diagenesis and Reservoir Quality. In: Houseknecht, D.W., Pittman, E.D. (Eds.), Origin, Diagenesis, and Petrophysics of Clay Minerals in Sandstones. SEPM Special Publication 47, pp. 227–240.

Kornman, B.A., De Deckere, E.M., 1998. Temporal variation in sediment erodibility and suspended sediment dynamics in the Dollard estuary. In: Black, K., Paterson, D.M., Cramp, A. (Eds.), Sedimentary Processes in the Intertidal Zone. Geological Society, London, Special Publications 139, pp. 231–241.

Leclair, S.F., Bridge, J.S., 2001. Quantitative interpretation of sedimentary structures formed by river dunes. J. Sediment. Res. 71, 713–716.

Lloyd, J.M., Zong, Y., Fish, P., Innes, J.B., 2013. Holocene and Lateglacial relative sea-level change in north-West England: Implications for glacial isostatic adjustment models. J. Quat. Sci. 28, 59–70.

Loizou, N., Andrews, I.J., Stoker, S.J., Cameron, D., 2006. West of Shetland revisited: The search for stratigraphic traps. In: Allen, M.R., Goffey, G.P., Morgan, R.K., Walker, I.M. (Eds.), The Deliberate Search for the Stratigraphic Trap. Geological Society Special Publication 254, pp. 225–245.

Manning, A.J., Langston, W.J., Jonas, P.J.C., 2010. A review of sediment dynamics in the Severn Estuary: Influence of flocculation. Mar. Pollut. Bull. 61, 37–51.

Matlack, K.S., Houseknecht, D.W., Applin, K.R., 1989. Emplacement of Clay into sand by Infiltration. J. Sediment. Res. 59, 77–87.

Molenaar, N., Felder, M., 2018. Clay cutans and the origin of illite rim cement: an example from the siliciclastic Rotliegend sandstone in the Dutch Southern Permian Basin. J. Sediment. Res. 88, 641–658.

Moraes, M.A.S., De Ros, L.F., 1990. Infiltrated clays in fluvial Jurassic sandstones of Reconcavo Basin, Northeastern Brazil. J. Sediment. Petrol. 60, 809–819.

Muto, T., Yamagishi, C., Sekiguchi, T., Yokokawa, M., Parker, G., 2012. The hydraulic autogenesis of distinct cyclicity in delta foreset bedding: flume experiments. J. Sediment. Res. 82, 545–558.

Needham, S.J., Worden, R.H., McIlroy, D., 2005. Experimental production of clay rims by macrobiotic sediment ingestion and excretion processes. J. Sediment. Res. 75, 1028–1037.

Skarpeid, S.S., Churchill, J.M., Hilton, J.P.J., Izatt, C.N., Poole, M.T., 2018. The Knarr Field: A new development at the northern edge of the North Sea. In: Bowman, M., Levell, B. (Eds.), Petroleum Geology of NW Europe: 50 Years of Learning – Proceedings of the 8th Petroleum Geology Conference. Geological Society, London, Petroleum Geology Conference Series 8, pp. 445–454.

Storvoll, V., Bjørlykke, K., Karlsen, D., Saigal, G., 2002. Porosity preservation in reservoir sandstones due to grain-coating illite: a study of the Jurassic Garn Formation from the Kristin and Lavrans fields, offshore Mid-Norway. Mar. Pet. Geol. 19, 767–781.

Sullivan, M., Coombes, T., Imbert, P., Ahamdach-Demars, C., 1999. Reservoir quality and petrophysical evaluation of Paleocene sandstones in the West ofShetland area. In: Fleet, A.J., Boldy, S.A.R. (Eds.), Petroleum Geology of NW Europe: Proceedings of the 5th Conference. Geological Society, London, Geology Conference Series 5, pp. 627–633.

Talling, P.J., Masson, D.G., Sumner, E.J., Malgesini, G., 2012. Subaqueous sediment density flows: Depositional processes and deposit types. Sedimentology 59, 1937–2003.

Taylor, T.R., Giles, M.R., Hathon, L.A., Diggs, T.N., Braunsdorf, N.R., Birbiglia, G.V., Kittridge, M.G., MacAulay, C.I., Espejo, I.S., 2010. Sandstone diagenesis and reservoir quality prediction: Models, myths, and reality. Am. Assoc. Pet. Geol. Bull. 94, 1093–1132. https://doi.org/10.1306/04211009123.

Tolhurst, T.J., Riethmüller, R., Paterson, D.M., 2000. In situ versus laboratory analysis of sediment stability from intertidal mudflats. Cont. Shelf Res. 20, 1317–1334.

Verhagen, I.T.E., Baas, J.H., Jacinto, R.S., McCaffrey, W.D., Davies, A.G., 2013. A first classification scheme of flow-bed interaction for clay-laden density currents and soft substrates. Ocean Dyn. 63, 385–397.

Waldmann, S., Gaupp, R., 2016. Grain-rimming kaolinite in Permian Rotliegend reservoir rocks. Sediment. Geol. 335, 17–33.

Widdows, J., Brinsley, M., Elliott, M., 1998. Use of in situ flume to quantify particle flux (biodeposition rates and sediment erosion) for an intertidal mudflat in relation to changes in current velocity and benthic macrofauna in: Black, K., Paterson, D.M., Cramp, A. (Eds.), Sedimentary Processes in the Intertidal Zone. Geol. Soc. Lond., Spec. Publ. 139, 85–97.

Wilson, M.D., 1992. Inherited grain-rimming clays in sandstones from eolian and shelf environments: their origin and control on reservoir properties in: Houseknecht, D.W., Pittman, E.D. (Eds.), Origin, Diagenesis, and Petrophysics of Clay Minerals in Sandstones. SEPM Spec. Publ. 47, 209–225.

Winterwerp, J.C., 2002. On the flocculation and settling velocity of estuarine mud. Cont. Shelf Res. 22, 1339–1360.

Winterwerp, J.C., Wang, Z.B., Van der Kraaij, T., Verelst, K., Bijlsma, A., Meersschaut, Y., Sas, M., 2006. Flow velocity profiles in the lower Scheldt estuary. Ocean Dyn. 56, 284–294.

Wood, R., Black, L., Jaco, C., 1998. Measurements and preliminary modelling of current velocity over an intertidal mudflat, Humber estuary, UK. In: Black, K., Paterson, D.M., Cramp, A. (Eds.), Sedimentary Processes in the Intertidal Zone. Geological Society, London, Special Publications 139, pp. 167–175.

Wooldridge, L.J., Worden, R.H., Griffiths, J., Thompson, A., Chung, P., 2017a. Biofilm origin of clay-coated sand grains. Geology 45, 875–878.

Wooldridge, L.J., Worden, R.H., Griffiths, J., Utley, J.E., 2017b. Clay-coated sand grains in petroleum reservoirs: understanding their distribution via a modern analogue. J. Sediment. Res. 87, 338–352.

Wooldridge, L.J., Worden, R.H., Griffiths, J., Utley, J.E., 2018. The origin of clay-coated sand grains and sediment heterogeneity in tidal flats. Sediment. Geol. 373, 191–209.
Wooldridge, L.J., Worden, R.H., Griffiths, J., Utley, J.E., 2019a. Clay-coat diversity in marginal marine sediments. Sedimentology 66, 1118–1138.
Wooldridge, L.J., Worden, R.H., Griffiths, J., Utley, J.E., 2019b. How to quantify clay-coat grain coverage in modern and ancient sediments. J. Sediment. Res. 89, 135–146.
Worden, R.H., Morad, S., 2003. Clay minerals in sandstones: Controls on formation, distribution and evolution. In: Worden, R.H., Morad, S. (Eds.), Clay Mineral Cements in Sandstones. IAS Special Publication 34, pp. 3–42.
Worden, R.H., Needham, S.J., Cuadros, J., 2006. The worm gut; a natural clay mineral factory and a possible cause of diagenetic grain coats in sandstones. J. Geochem. Explor. 89, 428–431.
Worden, R. H. Griffiths, J., Wooldridge, L. J., Utley, J. E. P., Lawan, A. Y., Muhammed, D. D., Simon, N., Armitage, P. J. (in press) Chlorite in sandstones. Earth-Sci. Rev.